

Mechanistic Origin of Rafting in Precipitation-Strengthened Ni-Based Single Crystals: Competing Chemomechanical Mechanisms and a Phase Diagram

Yanfei Gao,^{1,*} Qingqing Ding,^{2,*} Hongbin Bei^{2,*}

¹Department of Materials Science and Engineering, University of Tennessee, Knoxville, TN 37996, USA

²School of Materials Science and Engineering, Zhejiang University, Hangzhou 310027, China

Abstract

Background: When subjected to tensile stress at elevated temperatures, precipitation-strengthened Ni-based single crystals exhibit the elongation in shape, coarsening in size, and more intriguingly rafting of the L1₂-structured γ' precipitates, accompanied by the formation of face-centered-cubic γ matrix bands oriented perpendicular or parallel to the loading direction. *Objective:* Existing modeling efforts predominantly emphasize Eshelby-type configurational forces, i.e., the reduction of elastic potential energy arising from elastic interactions and interfacial dislocations. However, these analyses are mainly for the precipitate elongation, while detailed kinetic analyses remain lacking and the Herring-type self-diffusional mechanisms are generally not incorporated. *Methods:* In this work, we establish a comprehensive chemomechanical framework that integrates both Eshelby and Herring formalisms. Guided by extensive experimental parametric studies spanning a wide range of temperatures and loading rates, a mechanistic phase diagram is identified that distinctly separates elongation and rafting regimes. *Conclusions:* Energetic and kinetic comparisons demonstrate that rafting is governed by a stress-gradient-controlled self-diffusional process, rather than by the Eshelby-type species-diffusional mechanism. This unified framework not only rationalizes the experimentally observed mechanistic phase diagram but also clarifies the distinct physical origins of elongation and rafting in Ni-based single-crystal superalloys.

Keywords: Rafting; γ/γ' superalloy; Eshelby vs Herring; chemomechanical framework

* Corresponding information: ygao7@utk.edu, qq_ding@zju.edu.cn, and hbei2018@zju.edu.cn

Introduction

Precipitation-strengthened Ni-based single crystals are commonly used for elevated temperature applications such as gas turbine blades in aircraft engines. Single crystalline materials can be processed by directional solidification, which avoids the commonly observed grain-boundary cavitation processes in polycrystalline counterparts. A densely populated array of $L1_2$ -structured γ' precipitates, e.g., 70% volume fraction, are embedded in the face-centered-cubic (FCC) γ matrix. The two phases have very low, but nontrivial, mismatch in lattice constants and elastic moduli. At high temperatures, the intermetallic precipitate phase provides the needed strength, while dislocations cannot easily glide or climb, and thus usually cluster on the phase boundaries. These synergistic effects contribute to the excellent creep resistance of such second-generation Ni-based superalloys. However, ever since early days of its development and utilization, the γ/γ' superalloy exhibits a notorious microstructural evolution, denoted as rafting [1-3]. That is, precipitates elongate and “rafts” develop normal to the uniaxial tensile direction (Type N; more commonly seen), or parallel (Type P). The corresponding creep resistance is degraded, and, moreover, rafting can exacerbate and accelerate micro-cracking or other damage processes under creep-fatigue-oxidation conditions [4,5]. It is obviously a critical task to fully understand the mechanisms governing the complex interactions of microstructural evolution and mechanical deformation.

Before delving into the mechanistic origin of rafting, we first show some representative observations by the scanning electron microscopy (SEM) images in Figs. 1 and 2, which are based on our extensive parametric studies of processing and testing conditions, as well as advanced characterizations [6-9]. In these recent works, the second-generation Ni-based superalloy has the composition of 4.2Cr-8.8Co-2.2Mo-9.0W-8.0Ta-2.3Re-0.5Nb-5.1Al-0.1Hf-Ni in wt.%. This is similar to the commercial products such as CMSX4 and DD6. Single crystal samples were prepared by the Bridgman method, with the typical $\langle 001 \rangle$ growth direction. The as-grown rods were solid solution treated with 1290 °C/1h + 1300 °C/2h + 1315 °C/2h + 1325 °C/4h + 1330 °C/4h/AC, and then followed by a two-step aging process (1120 °C/4h/AC + 870 °C/24h/AC). Tensile tests across a wide range of temperatures were conducted at a controlled strain rate. While experimental details are not reiterated here, it should be noted that the full microstructural evolution from room temperature (RT) to 1100 °C, with loading rate ranging from 10^{-1} to $2 \times 10^{-5} \text{ s}^{-1}$, and at interrupted strain levels, can be found in our previous experimental works [6-9]. These observations have found more salient features than previous works and thus motivate the construction of a “mechanistic phase diagram” in this work here. The corresponding stress-strain curves (not included for brevity) for Figs. 1 and 2 give the fracture strain of 20~25%, so that one can estimate the total testing time from the labeled strain rate.

Under the same loading rate of 10^{-3} s^{-1} and thus the total duration of ~250 s in Fig. 1, microstructural evolution depends sensitively on the temperature. The elongation of γ' precipitates increases from about 1.5

to 2 when temperature rises from 900 to 1100 °C. In Fig. 1(c), the γ' precipitates form percolated stripes, which alternate with the soft matrix γ phase. This is the Type-N rafting since these stripes are perpendicular to the $\langle 001 \rangle$ loading direction. Note the γ' phase is cuboid or prismatic-like with the principal crystallographic axes aligning with its edges. Since the temporal duration is the same, the contrasting behavior at these three different temperatures suggest the kinetic process obeys the Arrhenius dependence, but the detailed mechanisms are not directly known. On the other hand, observations in Fig. 2 were taken from the same temperature (so that diffusivity, mobility, or other kinetic parameters are not changing), but with different loading rates. In other words, the total duration of testing changes from a few to $\sim 10,000$ seconds. Note that this is a creeping material, so that the flow stress shows a strong strain-rate dependence. The corresponding stress information is contained in the figure caption. Under short-time loading, the elongation (aspect ratio in Fig. 3) is about 1.5 under a few seconds in Fig. 2(a) and saturates to about 2.0 under a few hundred seconds in Fig. 2(c). Upon the occurrence of rafting, the inter-precipitate space in the transverse direction vanishes, and, simultaneously, elongation in the longitudinal direction halts. The transition from elongation in (a)-(c) to rafting in (d)-(e) suggests a characteristic time for rafting of ~ 1000 s at 1050 °C.

Define the geometric parameters for γ and γ' phases in Fig. 3(a), and their ratios are assembled in Fig. 3(b) with respect to temperature but under a fixed loading rate of 10^{-3} s^{-1} . The thick solid curves correspond to the SEM images at fracture. Additional data at intermediate strain levels are included at 900 and 1100 °C (taken from [8]), which correspond nicely with the mere elongation in Fig. 1(a) and the rapid occurrence of rafting in Fig. 1(c). Representative SEM images in Figs. 1 and 2, as well as the quantitative data in Fig. 3(b), reveal that elongation and rafting are two distinct “modes” and are sensitive to temperature and loading rate (or equivalently temporal duration). When rafting occurs, γ' precipitates resemble a rigid “skeleton” while the inter-precipitate γ phase in transverse direction “drains” off. Consequently, our thorough parametric studies in [6-9] reveal the “mechanistic phase diagram” as shown in Fig. 3(c) and summarized in Table 1, whereas the boundary delineates the elongation vs rafting modes.

The primary objective of this work is to rationalize the underlying mechanisms for this newly discovered map in Fig. 3(c), which contains far more useful information than the present literature. In the following, the section of *Methods* first reviews the present understanding that is based on the energetic driving force of the Eshelby type. A complete chemomechanical framework is established which distinguishes the mechanistic origins for Eshelby versus Herring mechanisms, the latter providing the driving force from the stress gradients. The section of *Results* conducts the kinetic analysis and derives the characteristic time scale for rafting, which is further compared to our experiments in Figs. 1-3. The section of *Conclusions* emphasizes the importance of proper treatments of chemomechanics, which, together with

the complete experiments in a vast parametric space, results into the identification of the mechanistic origin of rafting in γ/γ' superalloy.

Methods

Elastic Case: In Eshelby micromechanics [10], considering an inclusion with a transformation strain of ε_{ij}^T and assuming the same elastic constants in inclusion and matrix phases, the total elastic potential energy is written as

$$\Pi = \underbrace{\left\{ \frac{1}{2} \int_{\Gamma_{all}} \sigma_{ij}^0 u_{i,j}^0 dV - \int_{S_{all}} T_i^0 u_i^0 dA \right\}}_{\text{from external field only}} + \underbrace{\left\{ -\frac{1}{2} \int_{\Gamma_{inclusion}} \sigma_{ij}^I \varepsilon_{ij}^T dV \right\}}_{\text{from transformation strain only}} + \underbrace{\left\{ - \int_{\Gamma_{inclusion}} \sigma_{ij}^0 \varepsilon_{ij}^T dV \right\}}_{\text{interaction of two fields}}, \quad (1)$$

with the stress tensor σ_{ij} , strain tensor ε_{ij} , displacement vector u_i . Throughout this work, Latin indices run from 1 to 3, and summation convention is implied for repeated indices. A comma indicates differentiation, e.g., $u_{i,j} = \partial u_i / \partial x_j$. Here we have two sets of elastic fields. The first one (denoted with superscript “0”) arises from the externally applied surface traction T_i^0 , corresponding to the first term in Eq. (1). Due to ε_{ij}^T in the inclusion, the resulting field is denoted with superscript “I”, which, if acting alone, gives the elastic potential energy as shown by the second term in Eq. (1). The third term is the interaction energy of the two fields, which is the mechanistic driving force in many stress-induced phase transformation phenomena (e.g., precipitation in [11] and martensite in [12]).

Despite the complexity in solving the elastic fields, an interesting solution is that, regardless of inclusion shape, as long as the transformation strain is diagonal (i.e., $\varepsilon_{11}^T = \varepsilon_{22}^T = \varepsilon_{33}^T = \delta$), the second term in Eq. (1) is always equal to $\frac{E\delta^2}{1-\nu} V_{inclusion}$ with the Young’s modulus E , Poisson’s ratio ν , and inclusion volume $V_{inclusion}$. The integrand in the third term in Eq. (1) is constant and thus the integral is independent of the shape. Therefore, an applied tension cannot result into the elongation of the precipitates. However, removing the assumption of same elastic constants can change this conclusion. For example, Johnson and Cahn [13] shows that if the second phase is more compliant than the matrix, the elongated shape is energetically more favorable than the symmetric one. With the accurate knowledge of lattice and modulus mismatches, one can compare the elastic potential energies of various shapes, thus giving rise to the energetic driving force for the morphological evolution. This is the essential idea adopted in classic works by Pineau [2], Johnson and Cahn [13], Socrate and Parks [14], and Nabarro et al. [15,16].

Since both γ and γ' phases are cubic lattices, the lattice mismatch can be defined as

$$\delta = \frac{2(a_{\gamma'} - a_{\gamma})}{a_{\gamma'} + a_{\gamma}} \quad (2)$$

where a is the lattice constant of FCC or $L1_2$ phases. Using the neutron diffraction technique, Huang et al. [17] accurately measured the lattice constants in the range of 800~1200 °C for CMSX-4 and similar superalloys. Since δ is very small, the diffraction peaks of these two phases overlap, but can be separated due to the deep penetration capability of neutron beam and the resulting bulk average of a large number of grains. It is found that a_{γ} is slightly larger than $a_{\gamma'}$, and $\delta \approx -(0.1\sim 0.3)\%$. The elastic constants of the two phases are very difficult to separate from bulk measurements. In Epishin et al. [18], the sonic resonance method is used to measure the overall elastic constants of CMSX-4. Those of the γ phase are taken from measurements above the γ' solvus, so that those of the γ' phase can be determined by inverting the Reuss-Voigt-Hill homogenization from the γ' volume fraction. The elastic constants, C_{11} , C_{12} , and C_{44} , of γ phase are slightly larger than those of γ' phase by a few percent. Solving the anisotropic elasticity boundary value problem is significantly complex, so that the following modulus mismatch is commonly used,

$$m = \frac{E_{\gamma'} - E_{\gamma}}{E_{\gamma}}, \quad (3)$$

where E should be taken as $C_{11} - C_{12}$. From measurements in [17] and [18], γ/γ' superalloys like CMSX-4 and ours in Figs. 1-3 have $\delta < 0$ and $m < 0$.

According to Nabarro et al. [15,16], the driving force for the morphological change is proportional to this product, $\sigma_{appl} \delta m$, where σ_{appl} is the applied tensile stress and δ and m are defined in Eqs. (2) and (3), respectively. Even with a nontrivial δ but $m=0$, there is no driving force for the shape change. Furthermore,

$$\text{Elongation in tensile direction:} \quad \sigma_{appl} m \delta > 0 \quad (4)$$

which exactly applies to our material under tension, and the elongation in Figs. 1 and 2 agree with this prediction. It should be noted that this criterion cannot be extended to the rafting regime, in which percolated stripes form, although such subtleties are often unrecognized.

Plastic Case: Dislocations cannot be seen from SEM images in Figs. 1 and 2. While not included here, transmission electron microscopy (TEM) observations from our parametric studies in [6-9] reveal the accumulation of dislocation arrays/loops on the γ/γ' phase boundary. Determining the microstructural evolution certainly requires the energetic contributions from such plastic deformation, as handled by at least three different ways in literature.

The first way is the criterion proposed by Arrell and Vallés [19], which compares the dislocation energy when the precipitate shape and dislocation configuration are changed. However, the scaling relationship of various energetic terms is not addressed here. It is noted that the elastic potential energy in

Eq. (1) scales as the inclusion volume, i.e., $E\delta^2L^3$, where the difference between L_x and L_y is not considered. Furthermore, δ may be reduced by the in-plane component of Burgers vector of the interface dislocation. The interface energy scales as $\gamma_s L^2$ with γ_s being the phase boundary energy per unit area.

The interface dislocations give an energy that scales as $E \frac{b^2 L^2}{\lambda} \ln \frac{L}{r_{cutoff}}$, where b is the Burgers vector, λ is the dislocation spacing, and r_{cutoff} is a short-range cutoff radius [20]. Additionally, an interaction energy term exists due to the work done by the elastic fields from Eq. (1) on these dislocations. An energetic analysis, if missing the above size dependence and various energies, will become elusive.

In the works by Socrate and Parks [14] and Nabarro et al. [15,16], plasticity is not introduced through an explicit dislocation energy term, but treated as an anelastic, effectively reversible strain whose influence enters the problem through the Eshelby configurational force acting on the γ/γ' interfaces. The derivation is based on the Eshelby energy-momentum tensor [21] and will not be elaborated here. A configurational force per unit area and normal to the interface is

$$F = \llbracket W_e \rrbracket - T_i \llbracket u_{i,j} \rrbracket n_j, \quad (5)$$

where n_j is the interface normal (see Fig. 4 later), and the operator $\llbracket \dots \rrbracket$ denotes the discontinuous jump of the argument within. When an interface migrates during precipitate elongation, it sweeps through regions that have previously undergone plastic flow, thereby changing the work done by the external stress. Plasticity therefore modifies the driving force via the work term, i.e. the second one on the right hand side of Eq. (5), rather than by contributing directly to stored internal energy. In other words, the driving force changes from Eq. (4) to $-\sigma_{appl} \varepsilon_p$, with ε_p being the plastic strain next to the precipitates. This approach contrasts with that of Arrell and Vallés [19], who explicitly include dislocation storage energy in the free energy and treat plasticity as an irreversible, dissipative contribution to the thermodynamic driving force. The criterion in Eq. (4) is therefore modified as follows [14-16]. When the plastic strain just slightly exceeds $m\delta$, the plastic deformation in the matrix is rather complex near the precipitate phase, and where the initial plasticity takes place relies on the sign of $\sigma\delta$. Detailed simulations in Socrate and Parks [14] show that the precipitate will elongate transversely when $\sigma\delta < 0$ (e.g., the longitudinal elongation in our material should thus cease). Since the magnitudes of lattice mismatch and modulus mismatch are small, this criterion appears to be more applicable than the elastic one. However, there are two challenges here. Not only a direct comparison to our experimental observations in Figs. 1 and 2 fails to work as will be explained in details shortly, but also the matrix will quickly develop into a full plastic field or even creeping flow so that the elastic-plastic analyses in [14-16] may not apply.

Yet another approach to incorporate the plastic deformation is through the introduction of plastic work energy density, W_p , which is intended to account the contribution to the elastic distortion from the residual dislocations. Clearly, not only an extra relationship between dislocation density and plastic strain is required, but also the exact form of W_p differs throughout the literature. In the phase field formulation by Gaubert et al. [22], a mixed isotropic-kinematic hardening law is adopted for the soft γ phase, and W_p is taken from a temporal integral of the product of back stress and plastic strain rate. On the other hand, using a crystal plasticity formulation, Bower and Wininger [23] adopts the conventional product of resolved shear stress and crystalline slip rate, but multiplied by a Taylor-Quinney fractional factor so as to exclude other irreversible dissipative processes.

While the above formulations are often invoked to rationalize microstructural evolution in γ/γ' superalloy, our experimental parametric studies [6–9] show lots of features that cannot be explained in the classic framework, as compiled in Figs. 1-3. *First*, as shown in Fig. 3(c), a distinction between elongation and rafting clearly emerges. Note all data here are for approximately the same failure strain, so that the temporal duration is inversely proportional to the loading rate on the vertical axis. This newly discovered mechanistic phase diagram challenges all the above literature models, as predictions like in Eq. (4) are for elongation, but not for the percolated stripes in rafting.

Second, except for the phase field approach, the above models only provide an energetic driving force. That is, a comparison of the total free energy of various configurations suggests the equilibrium states, but no kinetic processes are explicitly specified. Therefore, a vast set of microstructural information with respect to time are not utilized in analyzing the validity of these models. The phase field approach (e.g., [22]) uses the functional derivative as the driving force, which is essentially the same as the Eshelby energy-momentum tensor formulation in Eq. (5), except the latter is for a sharp interface. The commonly used Cahn-Hilliard formulation in these phase field simulations implicitly assume that the kinetics is the diffusional rearrangement of the composition field, which is clearly the different molar fractions of Ni and Al in γ and γ' phases. Diffusivities in the intermetallic phase are much lower, and the species diffusivity of Al in γ , D_{Al}^γ , is at least one order or magnitude higher than that of Ni in γ , D_{Ni}^γ . Therefore, the time scale should be dictated by D_{Al}^γ , and the temperature dependence is given its corresponding Arrhenius relationship,

$$D_{Al}^\gamma = D_{Al,0}^\gamma \exp\left(-\frac{Q_{Al}^\gamma}{R_g T}\right), \quad (6)$$

where $D_{Al,0}^\gamma$ is a prefactor, R_g is the gas constant, and Q_{Al}^γ is the activation energy. However, the phase diagram in Fig. 3(c) points out that the kinetic processes for elongation and for rafting should differ. In

other words, the evolution of elongation is governed by Q_{Al}^γ in Eq. (6), but that of rafting by a different activation energy. When two Arrhenius relationships compete, their boundary can be described by a Zener-Holloman-type equation,

$$\dot{\epsilon}_{appl} \exp\left(\frac{Q_{rafting} - Q_{elongation}}{R_g T}\right) = const, \quad (7)$$

where $Q_{elongation} \approx Q_{Al}^\gamma$, and $Q_{rafting}$ is unknown for now but must be larger than $Q_{elongation}$ because of the positive slope of the boundary in Fig. 3(c).

Third, results in Figs. 1-3 provide additional validations to our hypothesis that the phase diagram should arise from two competing kinetic processes. Under intermediate temperature and high loading rate in Fig. 3(c), although there is a slight or moderate increase of dislocation density with respect to creep deformation, it is observed that the growth of γ' aspect ratio is not correlated closely to the plastic strain and the dominant elongation mode appears to be unaffected. More importantly, for the rafting mode under high temperature and low loading rate in Fig. 3(c), there is literally no change of dislocation density and network from TEM observations. The shape of γ' precipitates does not change noticeably, while the percolated γ stripe continues to thicken dramatically. This is the schematic drawing in the bottom right of Fig. 3(c).

Fourth, these superalloys are often doped with refractory elements to enhance the creep resistance. Under the Eshelby framework, it naturally follows that large elements like Re will segregate at the phase boundary, thus reducing the lattice misfit and the energetic driving force. Furthermore, Arrell and Vallés [19] and others suggest the possible role played by the segregation of other minor elements such as Cr and Re near the dislocations. But our energy dispersive X-ray spectroscopy (EDS) measurements disapprove such elemental redistribution. As shown in our example in [24], the compositions in the two phases remain largely unchanged before and after creep, while the Re element field change is related to the formation of topologically close-packed phases. Taken together, the above three points highlight the incompleteness of existing models and motivate the development of a comprehensive mechanistic study.

Chemomechanical Modeling Framework: Our method is based on the formulation in Bower and Wininger [23], but with further extensions to include the Eshelby configurational force [21] and the Herring formalism [25-29], as shown in Fig. 4. The interface normal \mathbf{n} and the tangential vector \mathbf{t} span a Cartesian coordinate that changes with respect to the arc length s . The chemical potential of atoms on the two sides of the interface is

$$\mu_{\pm} = \mu_{\pm}^0 + \Omega \left(\mp \frac{1}{2} \gamma_s \kappa + W_e + W_p - T_i u_{i,j} n_j - n_i \sigma_{ij} n_j \right), \quad (8)$$

where μ_{\pm}^0 are the reference values, Ω is atomic volume, κ is curvature (the two bodies see the opposite concavity), γ_s is the phase boundary energy per unit area, W_e and W_p are the elastic and plastic energy

densities as explained before, σ_{ij} is the stress field, $T_i = \sigma_{ij}n_j$ is the interface traction, and $\sigma_n = n_i\sigma_{ij}n_j$ is the normal stress. The linear dissipative law dictates the flux from the gradient of the chemical potential, i.e., $j = -M\nabla\mu$, where the mobility parameter M relates to a diffusivity parameter D through the Einstein-Nernst relationship, $M = \frac{D}{k_B T}$, with k_B being the Boltzmann constant.

The tangential flux of atoms along the phase boundary is therefore given by

$$j_{t\pm} = -\frac{D_{bt}\delta_b}{2k_B T} \frac{\partial\mu_{\pm}}{\partial s}, \quad (9)$$

$$j_t = j_{t+} + j_{t-} = -\frac{D_{bt}\delta_b}{k_B T} \frac{\partial[(\mu_+ + \mu_-)/2]}{\partial s} = -\frac{\Omega D_{bt}\delta_b}{k_B T} \frac{\partial}{\partial s} \left\{ \underbrace{(W_e + W_p - T_i u_{i,j} n_j)}_{\text{Energy term}} + \underbrace{(-\sigma_n)}_{\text{Herring term}} \right\}, \quad (10)$$

where D_{bt} is the tangential diffusivity along the phase boundary and δ_b is the total thickness of the diffusion layer. The flux of atoms from S^- to S^+ is

$$j_n = -\frac{D_{bn}}{k_B T} \frac{\mu_+ - \mu_-}{\Delta_n} = -\frac{\Omega D_{bn}}{k_B T \Delta_n} \left\{ \underbrace{(-\gamma_s \kappa)}_{\text{Gibbs-Thomson}} + \underbrace{[[W_e]] + [[W_p]] - T_i [[u_{i,j}]] n_j}_{\text{Energy-momentum tensor}} \right\}, \quad (11)$$

where D_{bn} is a diffusivity for the interface migration in the normal direction and Δ_n is an effective diffusion distance. A kinematic consideration gives the velocity of each side of the interface

$$v_{n\pm} = \pm \frac{\partial j_{t\pm}}{\partial s} - j_n. \quad (12)$$

Therefore, the normal velocity of the phase boundary is given by $\frac{1}{2}(v_{n+} + v_{n-}) = \frac{1}{2} \frac{\partial}{\partial s} (j_{t+} - j_{t-}) - j_n$, and the phase boundary thickening rate is $[[v_n]] = v_{n+} - v_{n-} = -\frac{\partial}{\partial s} (j_{t+} + j_{t-})$.

The various terms in Eqs. (8)-(11) are explained as follows. It should be reminded that the focus of this work is placed on the self-diffusion, so that the additional terms with respect to composition fields are not included in the above formulation. The term of $\gamma_s \kappa$ arises from the Gibbs-Thomson law. The Eshelby energy-momentum tensor [21] is derived from the functional derivative of the elastic potential energy with respect to a perturbed migration of the interface. Note that T_i and σ_n are continuous across the interface, but the jump of Eshelby energy-momentum tensor, $[[W_e]] - T_i [[u_{i,j}]] n_j$, is nontrivial. Adding $[[W_p]]$ is based on the extra deformation energy due to dislocations, but one can also use the approach in [14-16] by adding the plastic strain into the work term in Eq. (5). The Herring term should be explained as the additional work of adding one atom to (or inversely moving a vacancy away from) the location of interest [25]. Unlike the Eshelby term, one cannot derive it from the functional derivative from the elastic potential energy. We must

add this process into a variational framework, e.g., principle of virtual power [26]. The normal stress has no jump, so that it does not appear in Eq. (11).

The formulation of Eq. (10) can degenerate into several well-known problems. For example, a strained thin film can develop into wavy or island like surface morphology – a process called quantum dot formation. The free surface is traction free, so that the only remaining driving force in Eq. (10) is the elastic energy density. For another example, a cavity lying on the interface of two rigid grains can grow – a process denoted as the Hull-Rimmer mechanism. The rigid body assumption results into the only nontrivial driving force in Eq. (10) being the Herring term. Furthermore, the competition between Herring diffusion to dislocation creep is well explained in [26,27]. It also plays the critical role in “cold welding” nano-objects [28,29].

Lastly, for completeness, when dealing with self-diffusion in bulk, there is no discontinuous jump or curvature term. The bulk flux is essentially the same as Eq. (10), with the replacement of σ_n by the mean stress σ_{mean} .

Results

When using the chemomechanical framework in Fig. 4 to γ/γ' superalloy, it should be noted that the self-diffusion flux can be through the bulk (Location B to Location A) or along the phase boundary (Location B* to Location A*) as depicted in Fig. 5(a). To avoid complicated numerical simulations but still to capture the essential features, we use the schematic in Fig. 5(b) to justify why A and A* have higher tensile stress, so that their chemical potentials are lower according to Eq. (8).

The tensile deformation can be approximated by alternating two types of horizontal layers in longitudinal direction. The percolated γ phase forms a soft layer, while alternating γ and γ' phases in transverse direction forms the other type of layer. This distinction in Fig. 5(a) permits the simple analysis in Fig. 5(b). In situ neutron diffraction techniques can be used to obtain the lattice strain evolution of the constituent phases over a wide range of testing temperatures, from which the phase-specific stress-strain curves can be extracted [30]. Again, this is another unique set of experimental parametric studies that were unavailable when the classic elongation/rafting models were proposed. For brevity, we only draw the attention to the observation that the flow stress or creep strength of the γ' phase is much higher than that of the γ phase, thus leading to the schematic illustration in Fig. 5(b). The loading direction is in the iso-stress condition, so that $\sigma_A = \sigma_{appl}$. The longitudinal stress on the layer of γ/γ' is shared on the two phases in the iso-strain condition,

$$\sigma_B \left[1 - \left(\frac{L'_x}{L'_x + L_x} \right)^2 \right] + \sigma_C \left(\frac{L'_x}{L'_x + L_x} \right)^2 = \sigma_{appl}, \quad (13)$$

corresponding to the geometric construction by the vertical dashed line in Fig. 5(b). Thus, $\sigma_A > \sigma_B$.

The thinning of L_x^γ at Location B can be obtained from the Herring diffusion and a kinematic relationship,

$$L_y^\gamma \frac{dL_x^\gamma}{dt} = -\Omega L_x^\gamma j_{B \rightarrow A} \approx -\Omega L_x^\gamma \frac{D_{lattice}^\gamma}{k_B T} \frac{\sigma_A - \sigma_B}{L_y^\gamma}, \quad (14)$$

where $D_{lattice}^\gamma$ is the lattice diffusivity in the γ phase. The Herring diffusion from B^* to A^* follows Eq. (10), leading to the same representation but with a boundary diffusivity D_{bt} , instead of $D_{lattice}^\gamma$. Define an

effective diffusivity, $D_{eff}^\gamma = D_{lattice}^\gamma \left(1 + \frac{\delta_b}{L_x^\gamma} \frac{D_{bt}}{D_{lattice}^\gamma} \right)$. The solution is given by

$$L_x^\gamma = L_{x,0}^\gamma \exp\left(-\frac{t}{t^*}\right) = L_{x,0}^\gamma \exp\left[-\frac{\Omega}{k_B T} \cdot \frac{D_{eff}^\gamma (\sigma_A - \sigma_B)}{(L_y^\gamma)^2} \cdot t\right]. \quad (15)$$

The associated time scale can be estimated as follows. At 1050 °C, take D_{eff}^γ in the range of $10^{-15} \sim 10^{-14}$ m²/s, L_y^γ of about 0.5 μ m, $\sigma_A - \sigma_B$ of about 100 MPa since this strength difference is on the same order of magnitude as the overall strength [27], and Ω of about 10^{-29} m³ for Ni. The resulting t^* of about 1000s agrees nicely with the contrast between Figs. 2(c) and 2(d).

The phase diagram in Fig. 3(c) provides a clear illustration of the validity of both our chemomechanical modeling framework and the solution presented in Eq. (15), not through detailed parameter fitting, but rather via the elongation/rafting boundary described in Eq. (7). The following discussion is summarized in Table 1 for easy comparison.

Energetics: The Eshelby configurational force gives a local version, $[[W_e]] - T_i [[u_{i,j}]] n_j$, in Eq. (5), which can be integrated into our chemomechanical framework in Eq. (11). For the elongation mode, this leads to an overall version, $\sigma_{appl} m \delta$, by Nabarro et al. [15,16]. In contrast, the Herring formalism gives a local version, $-\sigma_n \Omega$ or $-\sigma_{mean} \Omega$, in Eq. (8). For the rafting mode, our analysis gives an overall version, $\sigma_A - \sigma_B$, which is a fraction of σ_{appl} from Fig. 5. As $m \delta$ is on the order of elastic strain, the Herring driving force is significantly larger than the Eshelby one. It should be reminded again that, as discussed in Fig. 4, some problems may only encounter the Eshelby configurational force (e.g., quantum dot formation), but some only see the Herring mechanism (e.g., Hull-Rimmer problem).

Kinetics: While not discussed in Nabarro et al. [15,16], the Eshelby configurational force is naturally embedded in the phase field model through the functional derivative. The use of Cahn-Hilliard

equation implies the diffusional transport of compositional fields, governed by Eq. (6). In contrast, the Herring process involves the lattice diffusivity. All the above discussions result into the following contrast

$$\text{Elongation: Species diffusivity} \times \text{Eshelby configurational force} \rightarrow D_{Al,0}^{\gamma} \exp\left(-\frac{Q_{Al}^{\gamma}}{R_g T}\right) \times \sigma_{appl} m \delta \quad (16)$$

$$\text{Rafting: Lattice diffusivity} \times \text{Herring driving force} \rightarrow D_{lattice,0}^{\gamma} \exp\left(-\frac{Q_{lattice}^{\gamma}}{R_g T}\right) \times (\sigma_A - \sigma_B) \quad (17)$$

Although the driving force in Eq. (16) is significantly smaller than that in Eq. (17), the species diffusivity D_{Al}^{γ} is in fact much larger than the bulk self-diffusivity $D_{lattice}^{\gamma}$. Note D_{Al}^{γ} is by Al atoms diffusing in Ni solid solution with measurements dated back to 1950s [31,32]. The commonly used diffusion-couple method (e.g., [33,34]) measures the Darken interdiffusion coefficient, $\tilde{D} = X_{Ni} D_{Al} + X_{Al} D_{Ni}$, where D_{Al}^{γ}

dominates. The lattice diffusivity, as suggested by Herring [25], is given by $D_{lattice} = \left(\frac{X_{Ni}}{D_{Ni}} + \frac{X_{Al}}{D_{Al}}\right)^{-1}$, where

D_{Ni}^{γ} dominates. Swalin and Martin [31] gives Q_{Al}^{γ} of about 64 kJ/mol, and Frost and Ashby [32] gives Q_{Ni}^{γ} of about 284 kJ/mol. Referring back to Eq. (7), it can be seen that $Q_{rafting} - Q_{elongation} \approx Q_{Ni}^{\gamma} - Q_{Al}^{\gamma}$ is about 200

kJ/mol, which is exactly the value used in the boundary curve in Fig. 3(c). This is the strongest evidence that validates our mechanistic interpretation in Eqs. (16) and (17). Furthermore, a combination between Eqs.

(16) and (17) gives the time ratio: $t_{Eshel}^* / t_{Herring}^* \approx \frac{D_{Ni,0}^{\gamma}}{m \delta D_{Al,0}^{\gamma}} \exp\left(-\frac{Q_{Ni}^{\gamma} - Q_{Al}^{\gamma}}{R_g T}\right)$. Since the modulus mismatch and the lattice mismatch are around one percent, the elongation-to-rafting transition in Fig. 3(c) occurs around 2000 s, and diffusivity prefactors are similar [31,32], this estimate nicely gives a prefactor of about 10^7 s^{-1} in the thick black curve in Fig. 3(c).

As a side note, the mechanism governing microcrack growth in Fig. 1 can be explained as follows. If these cracks extend by self-diffusion of atoms from crack tips to the crack surface, the analysis will be similar to the formulation in Eq. (8). The tensile stress concentration reduces the chemical potential. Using the classic Rice-Chuang solution for grain boundary cavitation [35] but noting that the ‘‘grain boundary’’ is really the percolated γ stripe, we obtain the associated time scale

$$\frac{1}{t_{crack}^*} = \frac{\Omega}{k_B T} \cdot \frac{D_{lattice}^{\gamma} L_y^{\gamma} \sigma_{appl}}{(crack\ size)^3}. \quad (18)$$

Comparing to the characteristic time for rafting in Eq. (15), we get $\frac{t_{crack}^*}{t^*} = \left(\frac{crack\ size}{L_y^{\gamma}}\right)^2$, so that the time

scale for diffusive crack growth is orders of magnitude higher than rafting. This mechanism is thus not

applicable in Fig. 1. An alternative mechanism is the plasticity-induced crack growth as in the Needleman-Rice solution [36,37], so that the time scale is simply inverse to the applied strain rate. Results in Fig. 1 show no dependence of these micro-cracks on temperature, and $1/\dot{\epsilon}_{app}$ being about 1000 s agrees well with these observations.

Conclusions

The classic rafting problem in γ/γ' superalloy is revisited, motivated by the identification of a mechanistic phase diagram, i.e., Fig. 3(c), derived from our recent experimental studies spanning a broad parametric space. Elongation and rafting modes are clearly distinguished, as our experiments demonstrate that at high temperatures and low loading rates, rafting occurs while γ' precipitate shapes remain essentially unchanged. The Eshelby configurational force considers only the reduction of elastic potential energy and is coupled with a species-diffusional process. In contrast, the Herring mechanism governs a self-diffusion flux from regions of low tensile/hydrostatic stress to regions of high stress, with the associated stress gradient arising from straightforward iso-stress and iso-strain constructions, as illustrated in Fig. 5(b). The corresponding kinetics is controlled by lattice diffusion. A comprehensive chemomechanical modeling framework integrating both formalisms is established in Fig. 4. Their competition, as quantified by Eqs. (16) and (17), leads to a Zener-Holloman-type relationship in Eq. (7) which matches remarkably well with the experimentally observed elongation/rafting boundary in Fig. 3(c).

Acknowledgements

YG is grateful to fruitful discussions with Profs. A.F. Bower, Z. Suo, and K. Zhao. QD and HB acknowledges support from the National Natural Science Foundation of China (No. 52571019, 52471019).

Ethical Approval

Not applicable.

Consent to Participate and Consent to Publish

Not applicable.

Competing Interests

The authors have no competing interests to declare that are relevant to the content of this article.

Author Contributions

Yanfei Gao, Qingqing Ding, and Hongbin Bei designed the project, conducted the investigation, and wrote the manuscript.

Funding

The National Natural Science Foundation of China (No. 52571019, 52471019).

Availability of Data and Materials

The original contributions presented in the study are included in the article; further inquiries can be directed to the corresponding author.

References

- [1] Tien JK, Copley SM (1971) The effect of uniaxial stress on the periodic morphology of coherent gamma prime precipitates in nickel-base superalloy crystals. *Metall. Trans.* 2:215-219.
- [2] Pineau A (1976) Influence of uniaxial stress on the morphology of coherent precipitates during coarsening – elastic energy considerations. *Acta Metall.* 24:559-564.
- [3] Pollock TM, Argon AS (1994) Directional coarsening in Nickel-base single crystals with high volume fractions of coherent precipitates. *Acta Metall. Mater.* 42:1859-1874.
- [4] Ding B, Ren W, Zhong Y, Yuan X, Zheng T, Shen Z, Guo Y, Li Q, Peng J, Brnic J, Gao YF, Liaw PK (2022) Revealing the influential mechanism of strain ranges on cyclic-life saturation during creep-fatigue in Nickel-based superalloy DZ445. *Int. J. Plast.* 155:103320.
- [5] Liu Z, Ding Q, Zhou Q, Yao X, Wei X, Zhao X, Wang Y, Zhang Z, Bei H (2023) The effect of oxidation on microstructures on a Ni-based single crystal superalloy during heat-treatment and simulated service conditions. *J. Mater. Sci.* 58:6343-6360.
- [6] Ding Q, Bei H, Zhao X, Gao Y, Zhang Z (2020) Processing, microstructures and mechanical properties of a Ni-based single crystal superalloy. *Crystals* 10:572.
- [7] Ding Q, Bei H, Li L, Ouyang J, Zhao X, Wei X, Zhang Z (2021) The dependence of stress and strain rate on the deformation behavior of a Ni-based single crystal superalloy at 1050 °C. *Int. J. Mech. Syst. Dynamics* 1:121-131.
- [8] Ding Q, Bei H, Yao X, Zhao X, Wei X, Wang J, Zhang Z (2021) Temperature effects on deformation substructures and mechanisms of a Ni-based single crystal superalloy. *Appl. Mater. Today* 23:101061.
- [9] Liu D, Ding Q, Zhou Q, Zhou D, Wei X, Zhao X, Zhang Z, Bei H (2023) Microstructure, mechanical properties and thermal stability of Ni-based single crystal superalloys with low specific weight. *Crystals* 13:610.
- [10] Eshelby JD (1957) The determination of the elastic field of an ellipsoidal inclusion, and related problems. *Proc. R. Soc. London A* 251:376–396.
- [11] Chen SY, Qiao J, Diao H, Yang T, Poplawsky J, Li W, Meng F, Tong Y, Jiang L, Liaw PK, Gao YF (2023) Extraordinary creep resistance in a non-equiatomically high-entropy alloy from the optimum solid-solution strengthening and stress-assisted precipitation process. *Acta Mater.* 244: 118600.
- [12] Xie D, Huang L, Shih HC, Tran H, Chew HB, Lyu Z, Liaw PK, Ren Y, Bower AF, Gao YF (2025) In situ synchrotron X-ray diffraction and crystal plasticity studies of the deformation and fatigue crack growth behavior in a TRIP-assisted advanced high strength steel. *Acta Mater.* 293:121122.

- [13] Johnson WC, Cahn JW (1984) Elastically induced shape bifurcations of inclusions. *Acta Metall.* 32:1925-1933.
- [14] Socrate S, Parks DM (1993) Numerical determination of the elastic driving force for directional coarsening in Ni-superalloys. *Acta Metall. Mater.* 41:2185-2209.
- [15] Nabarro FRN, Cress CM, Kotschy P (1996) The thermodynamic driving force for rafting in superalloys. *Acta Mater.* 44:3189-3198.
- [16] Nabarro FRN (1996) Rafting in superalloys. *Metall. Mater. Trans. A* 27:513-530.
- [17] Huang S, An K, Gao Y, Suzuki A (2018) Determination of γ/γ' lattice mismatch in Ni-based single-crystal superalloys at high temperatures by neutron diffraction. *Metall. Mater. Trans. A* 49:740-751.
- [18] Epishin A, Fedelich B, Finn M, Künecke G, Rehmer B, Nolze G, Leistner C, Petrushin N, Svetlov I (2021) Investigation of elastic properties of the single-crystal Nickel-base superalloy CMSX-4 in the temperature interval between room temperature and 1300 °C. *Crystals* 11:152.
- [19] Arrell DJ, Vallés JL (1994) Interfacial dislocation based criterion for the prediction of rafting behavior in superalloys. *Scripta Metall. Mater.* 30:149-153.
- [20] Gao Y, Larson BC (2015) Displacement fields and self-energies of circular and polygonal dislocation loops in homogeneous and layered anisotropic solids. *J. Mech. Phys. Solids* 83:104-128.
- [21] Eshelby JD (1975) The elastic energy-momentum tensor. *J. Elasticity* 5:321-335.
- [22] Gaubert A, Le Bouar Y, Finel A (2010) Coupling phase field and viscoplasticity to study rafting in Ni-based superalloys. *Phil. Mag.* 90:375-404.
- [23] Bower AF, Wininger E (2004) A two-dimensional finite element method for simulating the constitutive response and microstructure of polycrystals during high temperature plastic deformation. *J. Mech. Phys. Solids* 52:1289-1317.
- [24] Yao X, Ding Q, Wei, X, Zhang Z, Bei H (2024) The effect of stress gradient on the formation of topologically close packed phases in a Ni-based single crystal superalloy at 1050 °C. *Mater. Today Comm.* 40:109899.
- [25] Herring C (1950) Diffusional viscosity of a polycrystalline solid. *J. Appl. Phys.* 21:437-445.
- [26] Suo Z (2004) A continuum theory that couples creep and self-diffusion. *J. Appl. Mech.* 71:646-651.
- [27] Niu W, Gao Y (2021) Concomitant oxidation-diffusion-creep processes for stress generation and suppression of oxide-alloy interfacial instabilities. *J. Mech. Phys. Solids* 146:104218.
- [28] Dong P, Song B, Zhai X, Gao Y (2024) On the mechanistic origin of nanoscale “cold welding”. *Mater. Today* 80:905-912.

- [29] Song B., Dong P, Zhai X, Luo D, Gao Y (2025) A cold-welding map incorporating various competing mechanisms and size effects. *Scripta Mater.* 262:116646.
- [30] Huang S, Gao Y, An K, Zheng L, Wu W, Teng Z, Liaw PK (2015) Deformation mechanisms in a precipitation-strengthened ferritic superalloy revealed by in situ neutron diffraction studies at elevated temperatures. *Acta Mater.* 83:137-148.
- [31] Swalin RA, Martin A (1956) Solute diffusion in Nickel-base substitutional solid solutions. *JOM* 567-572.
- [32] Frost HJ, Ashby MF (1982) *Deformation Mechanism maps: the Plasticity and Creep of Metals and Ceramics.* Pergamon Press.
- [33] Rehman HU, Durst K, Neumeier S, Sato A, Reed R, Göken M (2017) On the temperature dependent strengthening of nickel by transition metal solutes. *Acta Mater.* 137:54-63.
- [34] Li Y, Ding Q, Wei X, Zhang Z, Gao Y, Bei H (2024) The effects of refractory elements on mechanical properties in CoCrNiFe concentrated solid solution alloys across different temperatures. *Materialia* 36:102187.
- [35] Chuang TJ, Kagawa KI, Rice JR, Sills LB (1979) Non-equilibrium models for diffusive cavitation of grain interfaces. *Acta Metall.* 27:265-284.
- [36] Needleman A, Rice JR (1980) Plastic creep flow effects in the diffusive cavitation of grain boundaries. *Acta Metall.* 28:1315-1332.
- [37] Zhang W, Gao Y, Feng Z, Wang X, Zhang S, Huang L, Huang Z, Jiang L (2020) Ductility limit diagrams for superplasticity and forging of high temperature polycrystalline materials. *Acta Mater.* 194:378-386.

Table 1: Competing chemomechanical mechanisms as a foundation for the mechanistic phase diagram in Fig. 3(c).

	Elongation Mode	Rafting Mode
Observations	γ' precipitates elongation (Type N or Type P)	γ phase forms percolated stripes
Energetic driving force	Eshelby configurational force (i.e., free energy reduction with respect to elongation)	Stress-gradient-driven self-diffusion
Kinetic process	Species diffusion; Ni and Al compositional change in γ	Lattice diffusion; primarily Ni atoms self-diffusing in γ
Activation energy	$Q'_{Al} \sim 64$ kJ/mol	$Q'_{Ni} \sim 284$ kJ/mol
Dominant parametric space	Intermediate temperature and high loading rate	High temperature and low loading rate

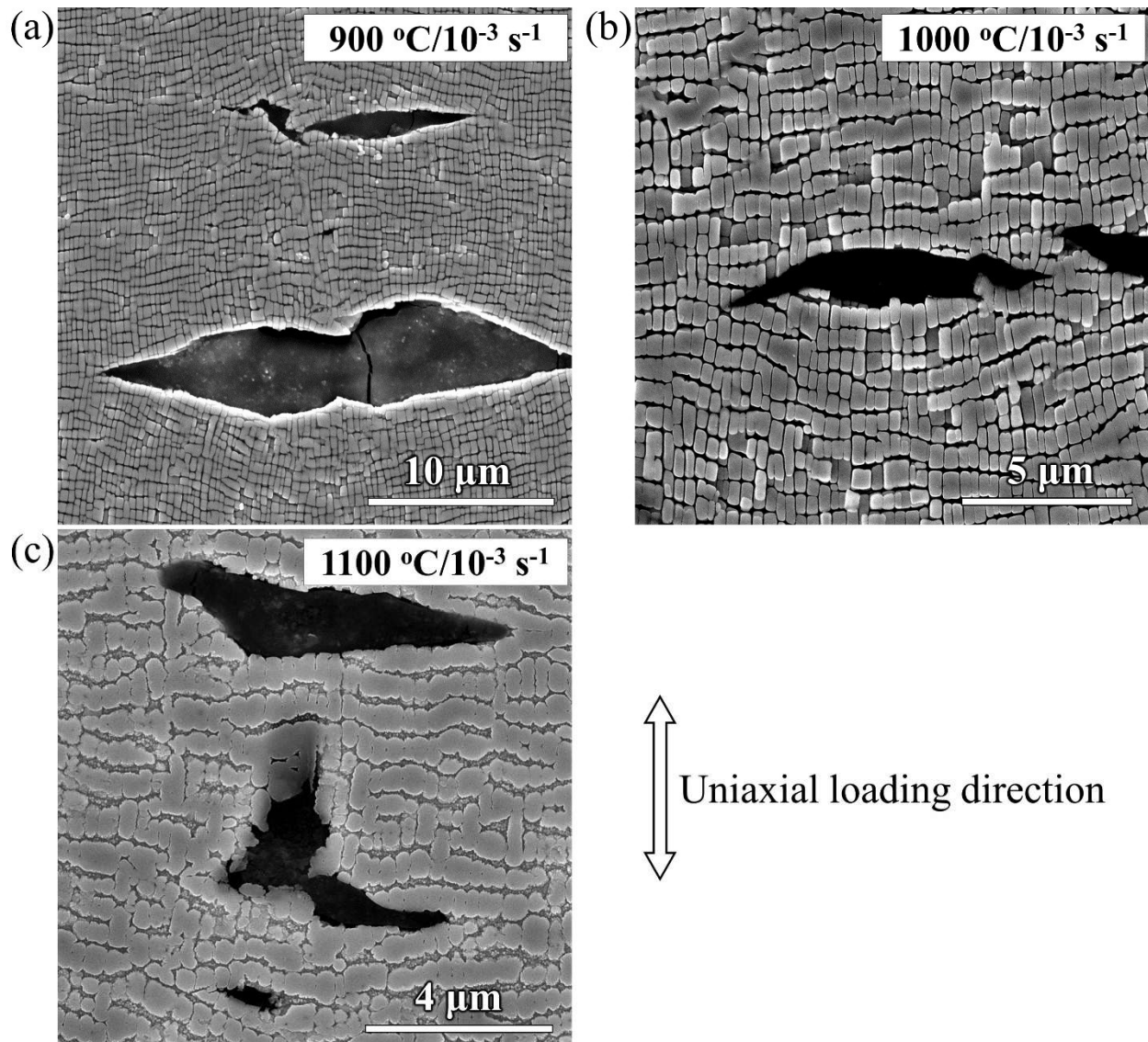


Figure 1: Selected SEM images of Ni-based γ/γ' single crystals at locations close to the final fracture surface. The tensile loading rate is 10^{-3} s^{-1} and the final fracture strain varies around 22~25% for all testing temperatures. Experimental details of SEM images see Ding et al. [6]. (a) 900 °C, loading time ~220 s, flow stress ~1000 MPa, and micro-crack sizes of 5~30 μm . (b) 1000 °C, loading time ~270 s, flow stress ~700 MPa, and micro-crack sizes of 10~40 μm . (c) 1100 °C, loading time ~260 s, flow stress ~400 MPa, and micro-crack sizes of 4~25 μm . The micro-crack sizes are not correlated with the temperature.

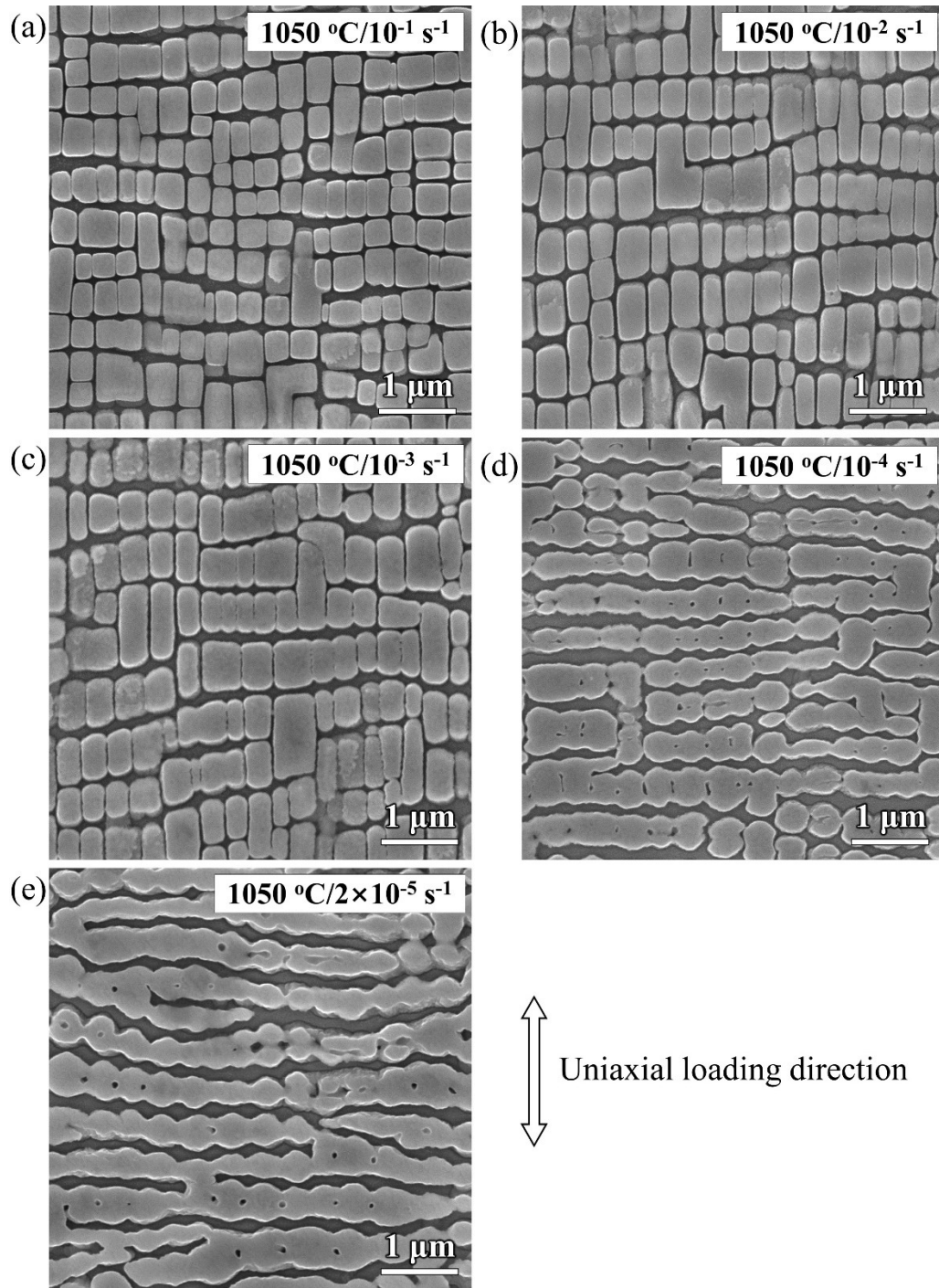


Figure 2: Selected SEM images of Ni-based γ/γ' single crystals at locations close to the final fracture surface. The testing temperature is fixed at 1050 °C with the loading rate labeled, and the final fracture strain varies again around 20~25%. Experimental details of SEM images see Ding et al. [7]. (a) 10^{-1} s^{-1} , loading time $\sim 2.2 \text{ s}$, and flow stress $\sim 850 \text{ MPa}$. (b) 10^{-2} s^{-1} , loading time $\sim 20 \text{ s}$, and flow stress $\sim 700 \text{ MPa}$. (c) 10^{-3} s^{-1} , loading time $\sim 200 \text{ s}$, and flow stress $\sim 550 \text{ MPa}$. (d) 10^{-4} s^{-1} , loading time $\sim 2000 \text{ s}$, and flow stress $\sim 450 \text{ MPa}$. (e) $2 \times 10^{-5} \text{ s}^{-1}$, loading time $\sim 10,000 \text{ s}$, and flow stress $\sim 400 \text{ MPa}$.

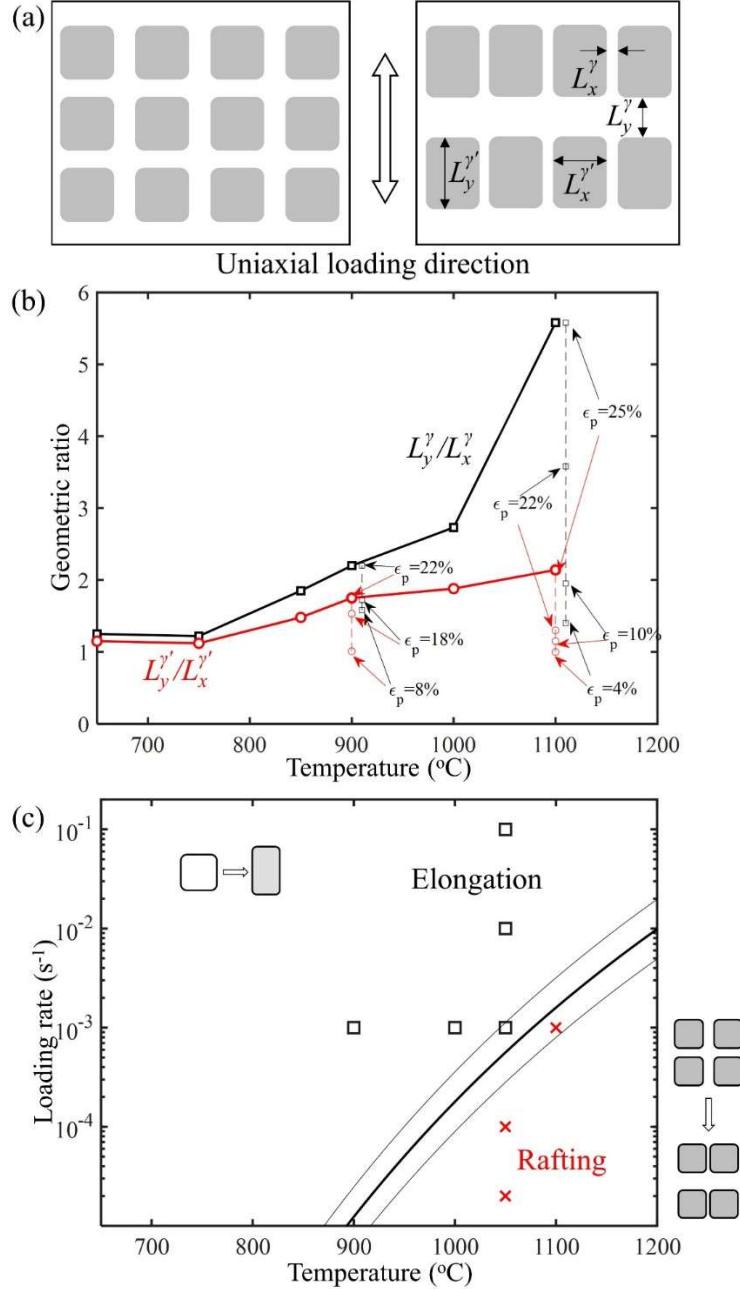


Figure 3: Dependence of elongation versus rafting modes on temperature and loading rate. (a) The definition of geometric parameters. The loading direction is in the y axis. (b) The thick solid curves indicate the geometric ratios at fracture. Furthermore, at 900 °C and 1100 °C, data with respect to the tensile plastic strain are also added. For clarity, the $L_y^{\gamma'}/L_x^{\gamma'}$ data are slightly shifted in the horizontal direction. All data were at a loading rate of 10^{-3} s^{-1} . Experimental details of SEM images see Ding et al. [6,8]. (c) Combining our parametric studies in [6-9], a clear “mechanistic phase diagram” emerges, whereas the three black curves correspond to the Zener-Holloman Eq. (7) with activation energy difference of 200 kJ/mol and constants being 2.5×10^6 , 5.0×10^6 (middle thick one), and 10^7 s^{-1} from bottom to top.

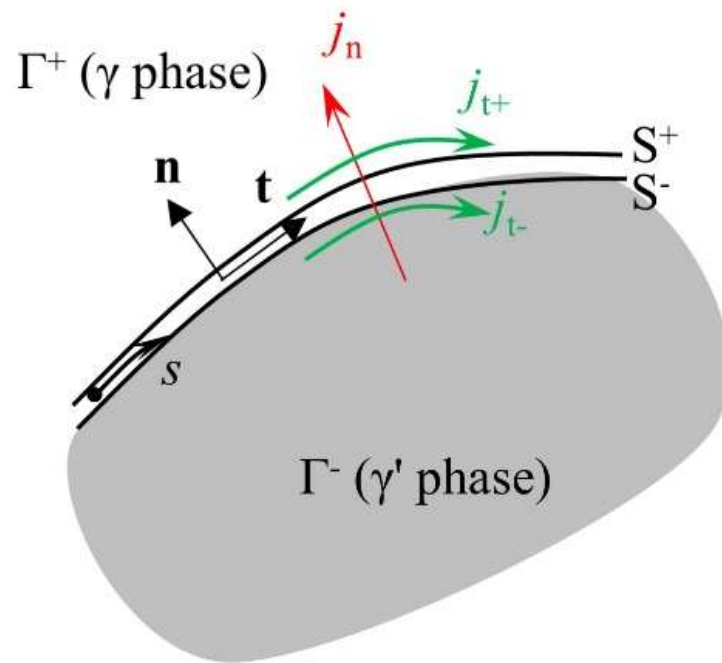


Figure 4: Schematic illustration of our chemomechanical modeling framework for the phase boundary. In the works of Socrate and Parks [14] and Nabarro et al. [15,16], the functional derivative of the total potential energy, i.e., the Eshelby configurational force, drives the interface migration. A distinct process is the Herring self-diffusion [25-29], which can take place at bulk or along interface.

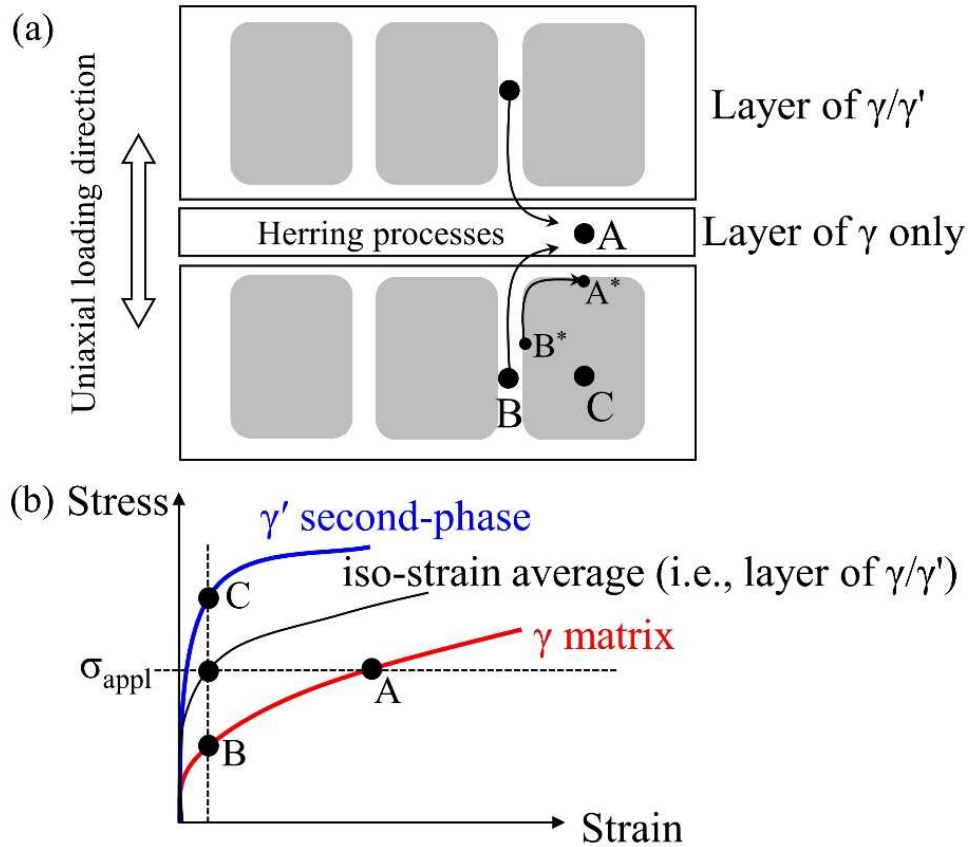


Figure 5: (a) The composite model used to rationalize the stress gradient. Self-diffusion can take place in the matrix γ -phase from Location B to Location A and in the phase boundary from Location B* to Location A*. (b) Schematic illustration of the stress-strain curves of individual phases and the iso-stress and iso-strain constructions. Under the uniaxial loading, the composite can be regarded as stacking the layers of γ -phase only and the layers of γ/γ' in series. This is the iso-stress condition, so that Location A is at the applied stress level. The layer of γ/γ' is approximately under iso-strain condition, so that the stresses in γ phase (Location B) and in γ' phase (Location C) differ.